Engineering Geology 292 (2021) 106249

Contents lists available at ScienceDirect

Engineering Geology

journal homepage: www.elsevier.com/locate/enggeo

GPR-inferred fracture aperture widening in response to a high-pressure tracer injection test at the Äspö Hard Rock Laboratory, Sweden

Justine Molron[a,c], Niklas Linde[b,*], Philippe Davy[c], Ludovic Baron[b], Caroline Darcel[a], Jan-Olof Selroos[d], Tanguy Le Borgne[c], Diane Doolaeghe[a,c]

[a] *Itasca Consultants S.A.S., 29 Avenue Joannès Masset, Lyon 69009, France*
[b] *Institute of Earth Sciences, University of Lausanne, Géopolis UNIL, Quartier Mouline, 1015 Lausanne, Switzerland*
[c] *Univ Rennes, CNRS, Géosciences Rennes, UMR 6118, 263 Avenue Général Leclerc, Rennes 35042, France*
[d] *Swedish Nuclear Fuel and Waste Management Company (SKB), Evenemangsgatan 13, Box 3091, SE-169 03 Solna, Sweden*

ARTICLE INFO

Keywords:
Ground penetrating radar
Surface-based method
Fracture
Tunnel
Nuclear waste disposal
High-pressure injection
Tracer test
Hydromechanics

ABSTRACT

We assess the performance of the Ground Penetrating Radar (GPR) method in fractured rock formations of very low transmissivity (e.g. $T \approx 10^{-9}$–10^{-10} m^2/s for sub-mm apertures) and, more specifically, to image fracture widening induced by high-pressure injections. A field-scale experiment was conducted at the Äspö Hard Rock Laboratory (Sweden) in a tunnel situated at 410 m depth. The tracer test was performed within the most transmissive sections of two boreholes separated by 4.2 m. The electrically resistive tracer solution composed of deionized water and Uranine was expected to lead to decreasing GPR reflections with respect to the saline in situ formation water. The injection pressure was 5000 kPa leading to an injection rate of 8.6 mL/min (at steady state) that was maintained during 25 h, which resulted in a total injected volume of 13 L. To evaluate the fracture pathways between the boreholes, we conducted 3-D surface-based GPR surveys before and at the end of the tracer tests, using 160 MHz and 450 MHz antennas. Difference GPR data between the two acquisitions highlight an increasing fracture reflectivity in-between the boreholes at depths corresponding to the injection interval. GPR-based modeling suggests that the observed increasing reflectivity is not due to the tracer solution, but rather to a 50% widening of the fracture. Considering prevailing uncertainties in material properties, a hydromechanical analysis suggests that such a degree of widening is feasible. This research demonstrates that field-scale in situ GPR experiments may provide constraints on fracture widening by high-pressure injection and could help to constrain field-scale elastic parameters in fractured rock.

1. Introduction

Characterization of flow and transport in fractured media presents important challenges. Flow in fractures is controlled by fracture aperture, fracture geometry and the connectivity between fractures forming a network (Gudmundsson, 2011). The high variability of these structural parameters results in complex preferential flow paths (Day-Lewis et al., 2017; Shakas et al., 2016; Tsang and Neretnieks, 1998; Tsang and Tsang, 1989; Tsoflias and Becker, 2008) with channelized transport (Klepikova et al., 2016; National Research Council, 1996) that enhances contaminant transport and makes remediation of contaminated sites extremely difficult (National Research Council, 1996; Neuman, 2005). The ability to obtain quantitative data, in situ, on flow paths and on hydraulic and hydromechanical properties is a prerequisite to understand such systems and to develop reliable predictive models (Selroos et al., 2002). The combined use of hydraulic tests and geophysical monitoring may offer such data at appropriate scales (Day-Lewis et al., 2017). In this paper, we carried out a tracer experiment with GPR monitoring in a low-permeability formation at depth to detect and quantify the spatial and hydraulic properties of a fractured system. An originality of this study resides in an attempt to quantify the evolution of the hydraulic properties under injection pressure in relation to the hydromechanical response of these fractured geological formations (Rutqvist et al., 1998; Zang et al., 2016).

Time-lapse ground penetrating radar (GPR) data can offer dynamic imaging, at high spatial resolution, of tracer transport in fractured media

---

[*] Corresponding author at: Institute of Earth Sciences, University of Lausanne, Géopolis UNIL, Quartier Mouline, 1015 Lausanne, Switzerland.

E-mail addresses: j.molron@itasca.fr (J. Molron), niklas.linde@unil.ch (N. Linde), philippe.davy@univ-rennes1.fr (P. Davy), ludovic.baron@unil.ch (L. Baron), c.darcel@itasca.fr (C. Darcel), jan-olof.selroos@skb.se (J.-O. Selroos), tanguy.le-borgne@univ-rennes1.fr (T. Le Borgne), d.doolaeghe@itasca.fr (D. Doolaeghe).

https://doi.org/10.1016/j.enggeo.2021.106249
Received 21 January 2021; Received in revised form 25 May 2021; Accepted 25 June 2021

(Becker and Tsoflias, 2010; Day-Lewis et al., 2003; Dorn et al., 2011a; Dorn et al., 2011b; Giertzuch et al., 2020; Shakas et al., 2016; Shakas et al., 2020; Talley et al., 2005; Tsoflias and Becker, 2008). The antenna frequency affects the sensitivity to fluid conductivity (Day-Lewis et al., 2003; Talley et al., 2005; Tsoflias et al., 2001) and fracture aperture (Tsoflias and Becker, 2008). Low to intermediate frequencies (25–200 MHz) have high sensitivities to electrical conductivity changes showing an increasing reflection coefficient when electrical conductivity increases (e.g., in response to a salt tracer injection). Higher frequencies are more sensitive to fracture aperture variations showing an increasing reflection coefficient and phase shift when aperture increases (e.g., in response to aperture widening induced by a high injection pressure).

Time-lapse GPR has proven effective when applied in fractured media with hydraulic transmissivities reaching 10^{-3}–10^{-5} m^2/s corresponding to mm-scale fracture apertures (Dorn et al., 2011b; Shakas et al., 2016; Talley et al., 2005; Tsoflias and Becker, 2008) as well as in less permeable formations composed by sub-mm aperture fractures (Giertzuch et al., 2020). Typically, saline (i.e., electrically conductive) tracer injections at rates of L/min are performed in fractures with lower-salinity formation water (i.e., electrically less conductive). To our best knowledge, time-lapse GPR has not yet been tested in formations with very low hydraulic transmissivity (e.g. $\approx 10^{-9}$- 10^{-10} m^2/s).

This setting of very low hydraulic transmissivity is investigated in the context of long-term deep disposal of nuclear waste. Low permeable crystalline rocks at 400–600 m depth are or have been targeted for such repositories by countries such as Sweden (Milnes, 2002), Finland (McEwen and Äikäs, 2000) and Canada (Davison et al., 1994), as they offer long-term mechanical, chemical and hydrogeological stability and could act as a potential barrier to leakage of contaminants (Neuman, 2005). In this contribution, we acquired time-lapse surface-based GPR data during a tracer test in a tunnel located at 410 m depth in the Äspö Hard Rock Laboratory, Sweden. In this experiment, aperture variations due to the high water-injection pressure are expected (Rutqvist et al., 1998; Zang et al., 2016) with associated impacts on the time-lapse GPR data.

Our experiment aimed to address the following questions:

1) In very low-permeability fractured formations with apertures <0.1 mm, can time-lapse GPR data detect induced salinity or aperture variations?
2) Can GPR data be used to constrain hydromechanical models predicting aperture and permeability enhancement during high-pressure injection tests?
3) Is the time-lapse GPR method, when employed in such low-permeability environments, able to provide visual constraints on the connected fracture network between boreholes?

We performed 3-D GPR acquisitions before and at the end of the tracer test (Sections 2.2 and 3.2). We then compared the observed time-lapse differences with GPR modeling for prescribed conductivity or aperture variations (Section 4.1). We further predicted the expected fracture aperture enhancement given hydromechanical parameters and injection conditions (Section 4.2).

2. Experimental set-up and data processing

The Äspö Hard Rock Laboratory (Sweden) is an underground research laboratory situated on the Simpevarp peninsula, Sweden, reaching 450 m below the sea level. It was constructed starting in 1990 (Cosma et al., 2001; Hammarström and Olsson, 1996) by the Swedish Nuclear Fuel and Waste Management Company (SKB). The laboratory has been used to test and develop engineering methodologies. For instance, underground flow and transport characterization approaches have been developed (Selroos et al., 2002) that account for the associated chemical reactions to better constrain potential future radionuclide migration and reactions. Methodologies and procedures developed at Äspö Hard Rock Laboratory will subsequently be used in the development of the planned Swedish nuclear waste repository (situated at Forsmark). Along the main tunnel (3.6 km long), several side-tunnels exist. The geology is mainly composed of fractured granitic rocks that are more than 1.7 billion years old (Cosma et al., 2001; SKB, 2016).

Our study tunnel, TAS04, is situated at 410 m depth with a length of 36 m, a width of 4.2 m and a height of 5.3 m. The main geological formations are composed by fine-grained granite, diorite and granodiorite. A 0.5 m thick portion of the original tunnel floor was cut and sawed by a diamond wire along 20 m to remove the fractures induced by the drill-and-blast excavation method (Ericsson et al., 2015; Ericsson et al., 2018). The resulting tunnel floor is flat and near horizontal leading to perfect conditions for the surface-based GPR method. This method was previously used to provide the most suitable siting of three 9.5 m deep boreholes (BH1, BH2 and BH3) crossing most sub-horizontal fractures imaged by the GPR (Molron et al., 2020). These boreholes were used for the hydraulic and tracer experiments (Section 2.1).

2.1. Hydraulic and tracer experiment

The hydraulic transmissivity of the fractured granite around TAS04 was initially estimated by hydraulic experiments performed by injection and outflow tests in 1-m packed-off sections in the three boreholes (BH1 to BH3) (Fig. 1b). Only 5 of the 21 solicited sections provided flows above the flowmeter threshold (2 mL/min) despite imposed pressure differences of 1000–2000 kPa. The total hydraulic transmissivities are 1.41×10^{-9}, 2.2×10^{-10} and 7.0×10^{-10} m^2/s for BH1, BH2 and BH3 respectively. For more details, see Andersson and Ragvald (2021) and Molron et al. (2020).

The tracer test was performed November 6–7, 2018, between BH1 and BH2 using a convergent-dipole geometry (higher outflow than injection rate) at high-pressure injection conditions. The outflow (BH1; 3.0–6.0 m depth) and injection (BH2; 3.2–3.7 m depth) intervals were selected such that they correspond to the most transmissive zones in the boreholes. Double-packer systems were used to isolate them from other sections (Fig. 1). The injection device used is the EDZ-equipment (initially designed for injection tests in shallow boreholes to study the excavation damage zones) (Andersson and Ragvald, 2021), equipped by a data collector and control systems connected to water and nitrogen bottles, gathered on a trolley (Fig. 1a). The experiment proceeded by imposing a constant high pressure that pushes the tracer solution towards the packers via the connected hydraulic tubes, while precisely measuring the injection rate with a mass flow meter. Outflow from the recovery borehole was established by opening the inter-packer section to the atmospheric pressure (no pump was used). The electrical conductivity (EC) was continuously measured at the outflow location via an EC sensor connected to the data logger. The outflow was measured manually with a bucket as it was under the measurement limit of the flowmeter. The tracer solution was collected using a sampling machine equipped with a peristaltic pump that collected the outflowing solution at a constant flow into 19 mL tubes. The sampling period varied between 10 and 60 min during the tests. Given the saline formation water (EC $\approx$ 1.8 S/m) containing relict seawater, we used a resistive tracer (Uranine diluted in deionized water) to create an electrical contrast (lower EC) and, thereby, changes in GPR reflectivity. Due to the large transit time (two hours) of the tracer within the plastic tubes connecting the EDZ device and the injection section, we pre-filled the tubes and the injection borehole with the tracer solution ($C_0 = 0.97$ ppm). We then injected the solution during 25.6 h with a mean injection pressure of 5000 kPa (starting with 4000 kPa for the 3.3 first hours) (Fig. 2a) corresponding to a mean injected flow of 8.6 mL/min at steady state, implying a total injected volume of 13.3 L and an outflow of 20 mL/min.

2.2. GPR experiment

The 3-D GPR surveys were performed the day before (reference

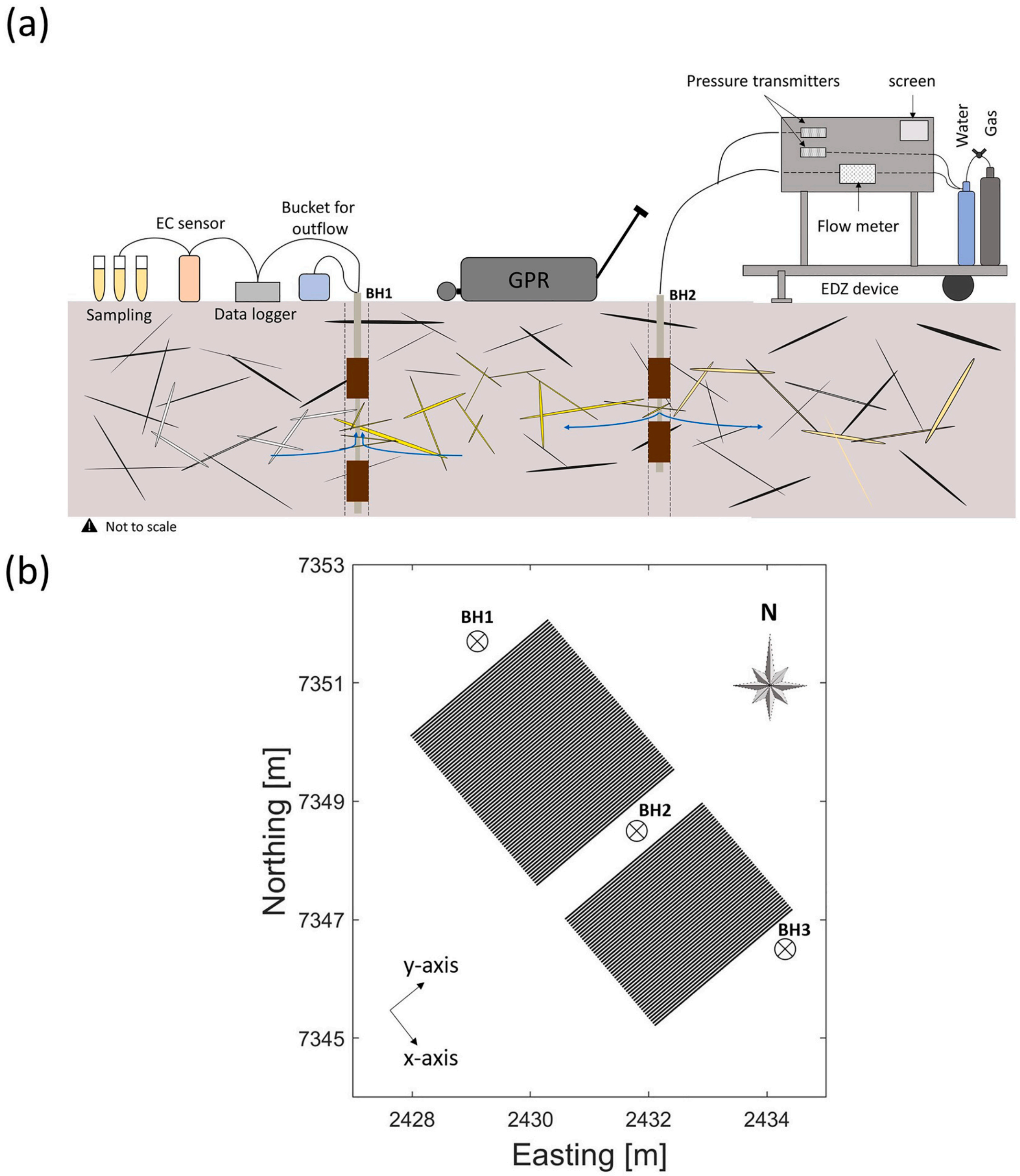

Fig. 1. (a) Schematic view of the experimental set-up (not to scale). A double packer system (in brown) is used to isolate the solicited borehole sections. The tracer solution is injected in BH2 by an EDZ-equipment with constant pressure and a flowmeter measuring the flow rate. The outflowing solution from BH1 is measured with an electrical conductivity (EC) sensor (connected to the data logger) and sampled. Surface-based GPR measurements were acquired before and during the tracer test. (b) 3-D GPR grid measurements in local Äspö96 coordinates in cross-line configuration following Molron et al. (2020) (along y-axis).

acquisition) and during the last hour (final acquisition) of the tracer experiment, in the period of November 5–7, 2018, using the MALÅ GroundExplorer (GX) HDR-series (High Dynamic Range). We used both 160 MHz and 450 MHz antennas to leverage their different sensitivities to the electrical conductivity of the fracture fluid and aperture (Tsoflias and Becker, 2008). The transmitter and receiver antennas are gathered in a shielded device that is pulled with a sledge on the cleaned and flat tunnel floor (surface-based method) using wooden planks and measurement tape to ensure straight parallel lines and a high degree of repeatability in terms of positioning between acquisitions. The separation between antennas is fixed (0.33 m and 0.18 m for 160 MHz and 450 MHz, respectively); a so-called common-offset configuration. The 3-D set-up geometry consists of many parallel lines in “cross-line configuration” using the terminology of Molron et al. (2020) (along the y-axis corresponding to the tunnel width direction) between the chosen boreholes and beyond the injection hole (Fig. 1b). A distance of 0.10 m and 0.05 m separated the profiles using 160 MHz and 450 MHz antennas, respectively. This resulted in 64 (160 MHz) and 129 (450 MHz) profiles covering an area of 3 m × 6.3 m (including a 0.65 m wide region without measurements due to the injection borehole instrumentation). The time-periods of the acquisitions with respect to the injection experiment are shown in Fig. 2a.

In a previous study in the same tunnel (Molron et al., 2020), the GPR data were processed to obtain images with magnitudes reflecting the spatially varying reflection coefficients of fractures. Furthermore, the processing workflow included a rather strong suppression of ringing events to avoid interpreting such artifacts as near-horizontal fractures. Based on the resulting images, it was then possible to identify the most prominent fracture reflections. In the present study, we are primarily interested in identifying the fractures showing the largest relative variations in reflectivity over time, as they are likely to correspond to changing aperture or electrical conductivity of the fluid-filled fractures

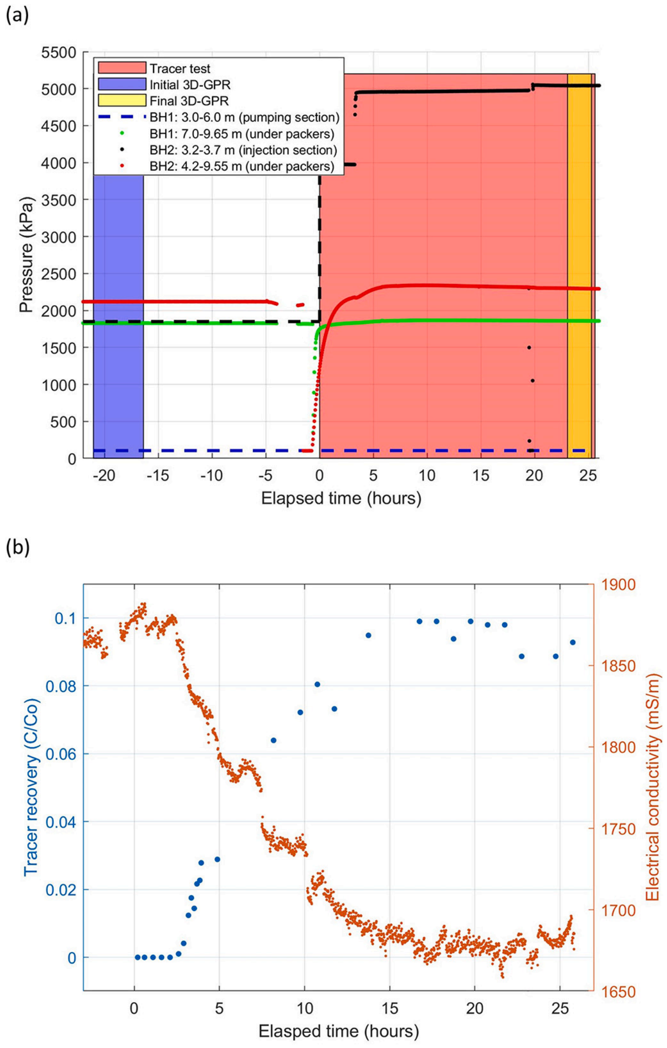

Fig. 2. (a) Pressure data before and after the injection below the double packers in BH1 (green) and BH2 (red) and in the injection section (black). The recovery section (blue dashed lines; not measured) was open to the atmosphere (14 days before and during the tracer tests). The reference and final GPR acquisition times and the injection times are represented in blue, yellow and red, respectively. (b) Tracer recovery (blue) and electrical conductivity of the outflowing water at the exit of BH1 (orange). (For interpretation of the references to colour in this figure legend, the reader is referred to the web version of this article.)

in response to the injection experiment. Hydrological data (Molron et al., 2020) indicate further that near-horizontal fracture pathways are likely. Time-lapse comparisons of traces make it easier to identify horizontal events than for static surveys as ringing effects are likely constant over time and can be removed by subtraction. Consequently, we decided to not remove horizontal events by applying, for example, singular value decomposition (SVD) when processing these data.

In the present study, GPR processing starts with an editing step that serves to prune additional traces of the GPR-profiles in order to obtain a rectangular measurement block. Direct current (DC) removal consists of removing data offsets and was here achieved by subtracting the median of the last 20% of the unnormalized GPR traces. The time zero correction corrects the signal initiation time based on the antenna separation and the speed of light in a vacuum. This is achieved by shifting the time vector using an amplitude threshold chosen to be slightly above the noise level and to attribute the first such occurrence to the first-arrival of the airwave. Subsequently, a high-pass zero-phase filter is used to remove low frequencies below 80 and 160 MHz, respectively. When performing time-lapse differencing, it is essential to overlay the traces carefully with respect to signal attributes that are assumed to be time-invariant (in our case, the first 8.9 and 3.5 ns of the signal for 160 and 450 MHz, respectively) in order to ensure that time-lapse differences refer to actual in situ variations. For accurate trace alignment, we are limited by the finite sampling rate of the GPR system and perform, thus, upsampling using a Fourier transform to a ten times higher sampling rate. The resulting traces acquired at the same location at different times are aligned and the energy is normalized in the identified time-windows before downsampling the signal to the original sampling rate for further analysis. To ensure a similar magnitude range throughout the 3-D data volume, we perform automatic gain control (AGC) using the reference data and apply the resulting gain function to the final acquisitions as well. In this way, it is possible to assess relative differences over time as the gain function remains constant. This AGC processing allows us to identify regions with small reflectivity, but large relative temporal variations. This is helpful as it is not necessarily the regions with the highest GPR reflectivity that are stimulated by our experiments. The data volumes acquired at different times are subtracted and differences observed are interpreted as being related to induced changes in the fractures or their fluids.

Lastly, we applied 3-D Kirchhoff migration (Margrave and Lamoureux, 2019) on the processed reference GPR acquisition data and the difference between processed GPR acquisitions (final - reference) to collapse the many diffractions and locate the GPR reflections at depth. This was achieved using the CREWES Matlab toolbox (CREWES, 1988) assuming a constant velocity of 0.125 m/ns, which provided the best collapse of the diffractions in the migrated images.

3. Results

3.1. Hydraulic data

The pressure conditions before and during the tracer test are depicted in Fig. 2a. In BH1, the packed-off interval was open to the tunnel through the outflow tube, implying near-atmospheric conditions while the pressure was around 1830 kPa below the double packer. In BH2, the pressure well-before injection was around 1850 kPa in the injection section and around 2120 kPa below the double packer. At 1.5 h before injection, the pressure in BH2 drops towards zero as the packer was momentarily deflated and filled with tracer solution. When injection started, the imposed pressure in BH2 was around 4000 kPa for the first three hours after which it was raised to 5000 kPa. A resulting minor pressure increase is observed below the packers in BH1 and BH2 at levels of 1860 kPa and 2230 kPa, respectively. The short decrease 19.8 h after the injection start in the injection interval was due to incorrect manipulation when closing the tracer bottle after the last refilling. The tracer recovery and its electrical conductivity are shown in Fig. 2b. The first tracer arrival in BH1 is sampled after 1.95 h of injection (after correcting for the transfer time of the tracer in the tubes). This time agrees with the time of the initial drop in electrical conductivity measured by the EC sensor.

3.2. GPR data

Fig. 3 presents horizontal visualizations of the processed 450 MHz 3-D GPR data for the reference acquisition (before the injection) (Fig. 3a–c), the final acquisition (after injection) (Fig. 3d–f), for data differences (final – reference) (Fig. 3g–i) and migrated difference-data (Fig. 3j–l). We selected three depths (2.5 m, 3.6 m and 4.3 m) corresponding respectively to one depth level above, one within and one below the injection interval. This was done to observe the behavior of the GPR signals at depths presumably affected (3.6 m) or unaffected (2.5 m and 4.3 m) by the tracer test. At 2.5 m depth (above the injection section), the structures featured in the reference (Fig. 3a) and final data (Fig. 3d) disappear in the difference data and in the resulting difference

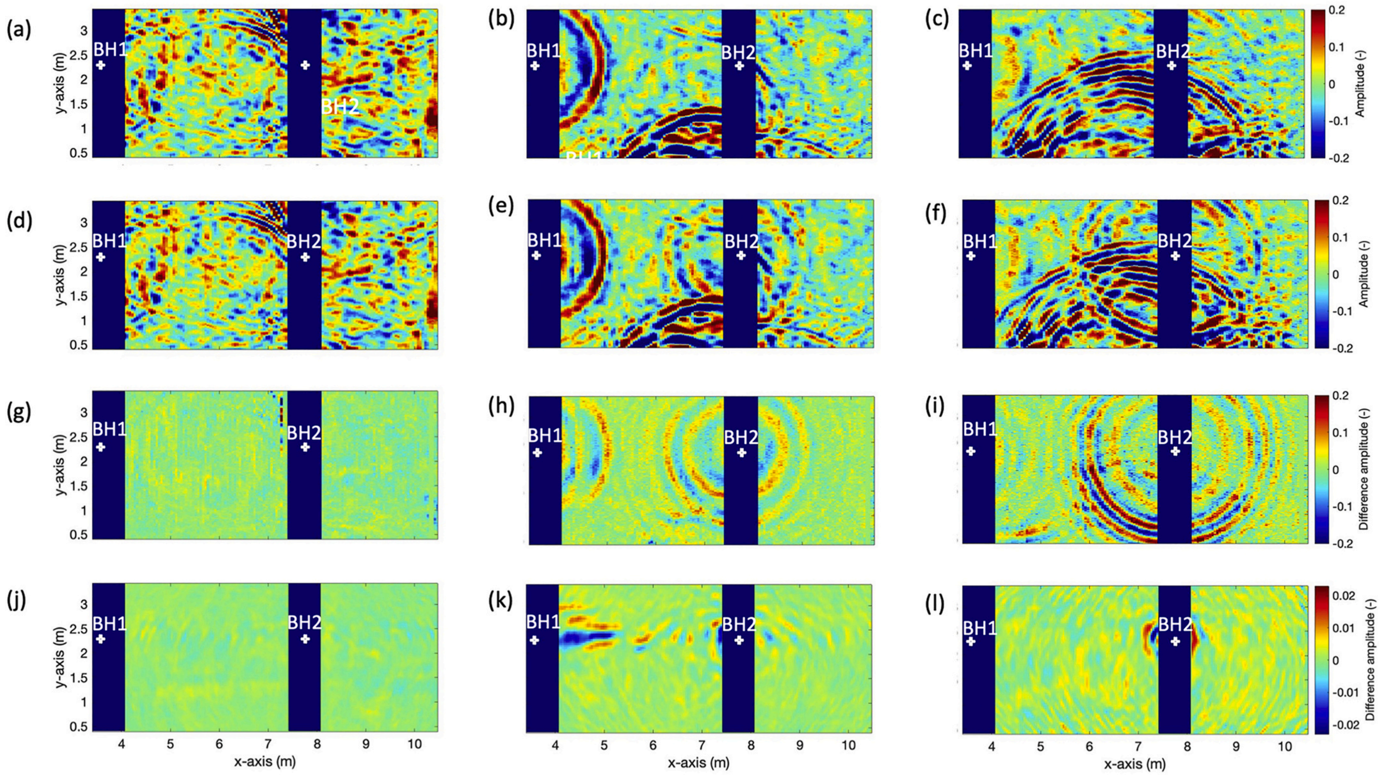

Fig. 3. Depth slices of 3-D GPR measurements (450 MHz) at 2.5 m (a,d,g,j), 3.6 m (b,e,h,k) and 4.3 m (c,f,I,l) depth. (a,b,c,) the time-to-depth converted processed data before injection (reference), (d,e,f,) the time-to-depth converted processed data after injection (final), (g,h,i) the difference between time-to-depth converted processed data (final - reference) and (j,k,l) the migrated difference-data (final - reference).

migration results (Fig. 3g, j). The very strong similarity between the reference data (Fig. 3a) and the final data (Fig. 3d) at this depth interval suggests that high repeatability in terms of positioning and the GPR processing procedure allow for highly comparable acquisitions. Indeed, even minute positioning or amplitude errors would have shown up in the difference image (Fig. 3g). At 3.6 m depth (within the injection section from 3.2 to 3.7 m), the structures resulting from the processed difference data (Fig. 3h) correspond to diffraction-like events close to the boreholes. As we were unable to measure GPR data above the boreholes, it is difficult to establish the exact origin of these time-lapse differences. One possibility is that the diffractions associated with the metallic parts of the packers vary as the injection borehole was filled by highly conductive formation water during the reference acquisition and by resistive tracer solution during the final acquisition.

After difference migration, the borehole-related diffractions have largely collapsed and leave features aligned along a linear path connecting the injection and extraction borehole (Fig. 3k). Despite that most diffractions were collapsed, residual energy still remain around the injection borehole. This can be explained by the lack of measurements above the boreholes. At 4.3 m depth, only diffractions are observed on the unmigrated difference-data (Fig. 3i) and they are mostly collapsed in the migrated difference-data (Fig. 3l). By studying the migrated difference-data at these depth intervals, we observe that coherent time-lapse differences away from the injection region appear only in the depth range at which we are injecting tracer and expect the tracer transport to take place.

The 3-D migrated reference (Fig. 4a) and difference-data (Fig. 4b) were imported into the software Paradigm GOCAD™. The "inline" (*x*-direction) vertical profile showed is an interpolation of the 129 cross-line profiles (*y*-direction) that were acquired. The term in-line is here used to be in agreement with Molron et al. (2020). The structures highlighted on Fig. 3h are well visible at depths of 3.6 and 3.4 m between the solicited borehole sections (in yellow), and are well distinguished from the background signal.

Exemplary 3-D 160 MHz migration results are also given for the reference (Fig. 5a) and difference data (Fig. 5b). Compared to the 450 MHz data, we observe that more of the structures seen in the reference acquisition are left in the migrated difference-data, making data interpretation more challenging. The long patterns remaining after the differencing may suggest an origin from the surface. We used wooden planks to ensure straight parallel lines of the 3-D GPR measurements. These planks were dry during the reference acquisition and wet during the final acquisition. Consequently, we cannot exclude different coupling between the antennas and the wooden planks that might have changed the effective wavelet in a way that we could not correct for with our processing scheme. Generally speaking, the 160 MHz data by Molron et al. (2020) had a much more "ringy" character than the 450 MHz data that was removed by an SVD-based processing step. However, no such step was applied here as we wanted to localize flow paths that were expected to be largely sub-horizontal. Despite these noisy structures, we observe similar patterns connecting BH1 and BH2 in the injection depth area (inter-packer section represented in yellow) (Fig. 5b).

4. Discussion

4.1. GPR-based scenario modeling

Except for the area around the injection borehole (BH2) that is influenced by non-collapsed diffractions, we are able to identify fractures that are affected by the tracer injection on difference migrated 2-D profiles of 450 MHz data (Fig. 4b). It is more difficult to observe these linear reflections on 160 MHz migrated difference-data (Fig. 5b) due to the superimposed horizontal ringing patterns, but some coherent reflection trends are seen at the injection depth level. We analyzed the temporal variation of the amplitudes (Fig. 6) and focus on two regions of temporal variations. These regions in-between the boreholes close to the

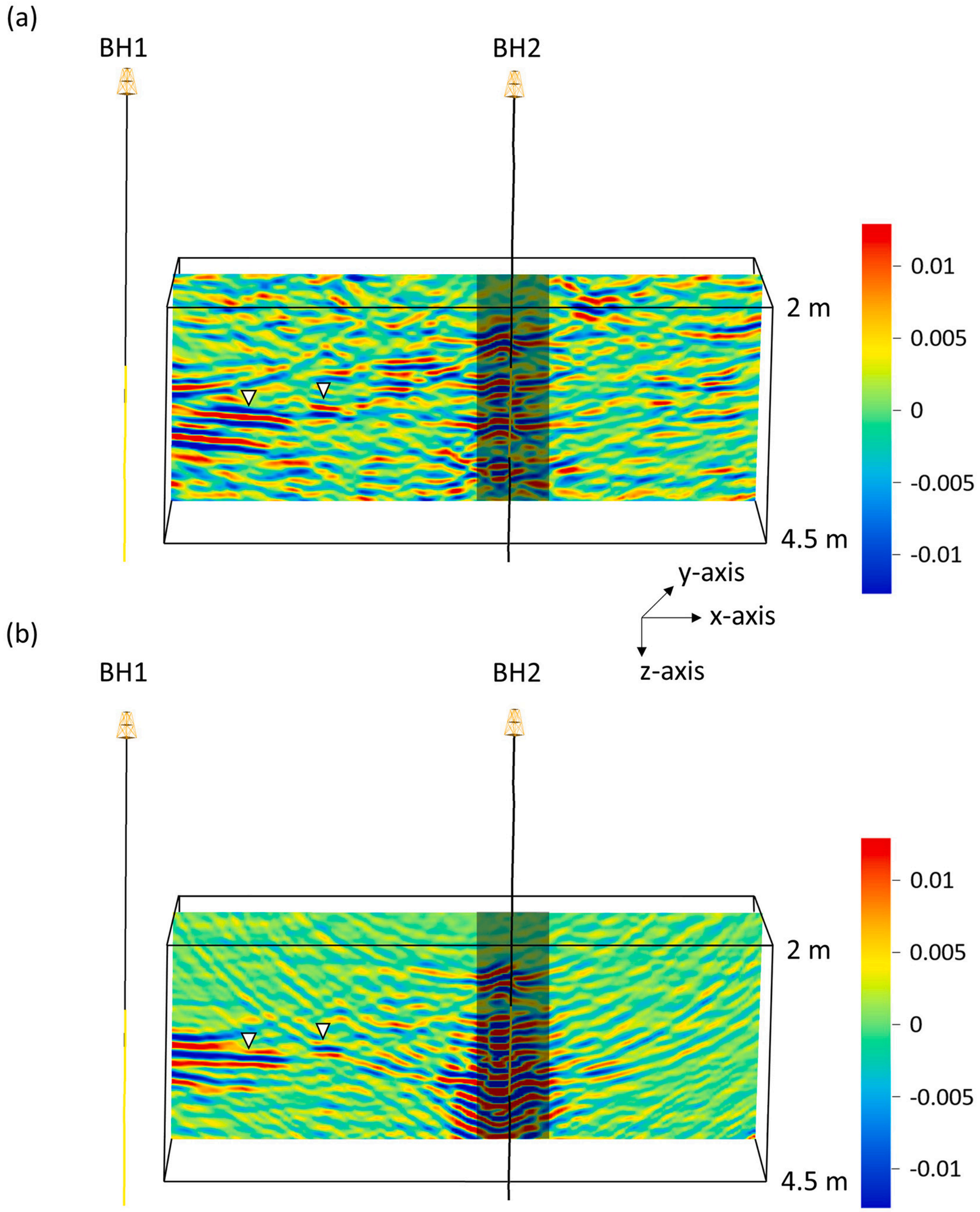

Fig. 4. 3-D migrated 450 MHz data represented by a vertical slice passing through the chosen boreholes. (a) Migration of the processed reference GPR acquisition data (before injection) and (b) migration of difference-data (final – reference). The shaded area corresponds to the zone above which we did not perform GPR profile surveys. The injection and extraction boreholes are BH2 and BH1, respectively, with the solicited sections highlighted in yellow along the boreholes. The apexes of white triangles indicate the location of observed relative amplitude changes that are analyzed in Section 4.1 (Fig. 6c, d). The amplitudes are unitless and refer to the input data for migration that had normalized magnitudes varying between −1 and 1. (For interpretation of the references to colour in this figure legend, the reader is referred to the web version of this article.)

injection depth (indicated in Figs. 4 and 5 by triangles) are considered to originate from two separate fractures. They are situated at 3.6 m (Fig. 6a, c) and 3.4 m (Fig. 6b, d) depth, at 1.14 m and 2.18 m away from BH1 respectively. The time-lapse differences of these two migrated signals reveal an increase of the reflection magnitude for both frequencies, only at these depth regions.

To understand the possible origin of these temporal variations, we modeled GPR signals from a fracture with varying electrical conductivity and fracture aperture. To do so, we used the semi-analytical, frequency-domain-based, effective-dipole forward modeling approach by Shakas and Linde (2015). In this approach, a fracture of prescribed size and orientation (dip and strike) is discretized by squares at a scale that is several times smaller than the dominant wavelength. The source radiation in a uniform isotropic rock matrix with prescribed electrical properties is calculated analytically, assuming an infinitesimal dipole and a prescribed source wavelet, from which the tangential component of the electrical field is recorded at the center of each discretized element. Using this information, the area of the discretized element, and assumed fracture properties (electrical conductivity and permittivity of the fracture filling) together with the thin-bed solution, it is possible to

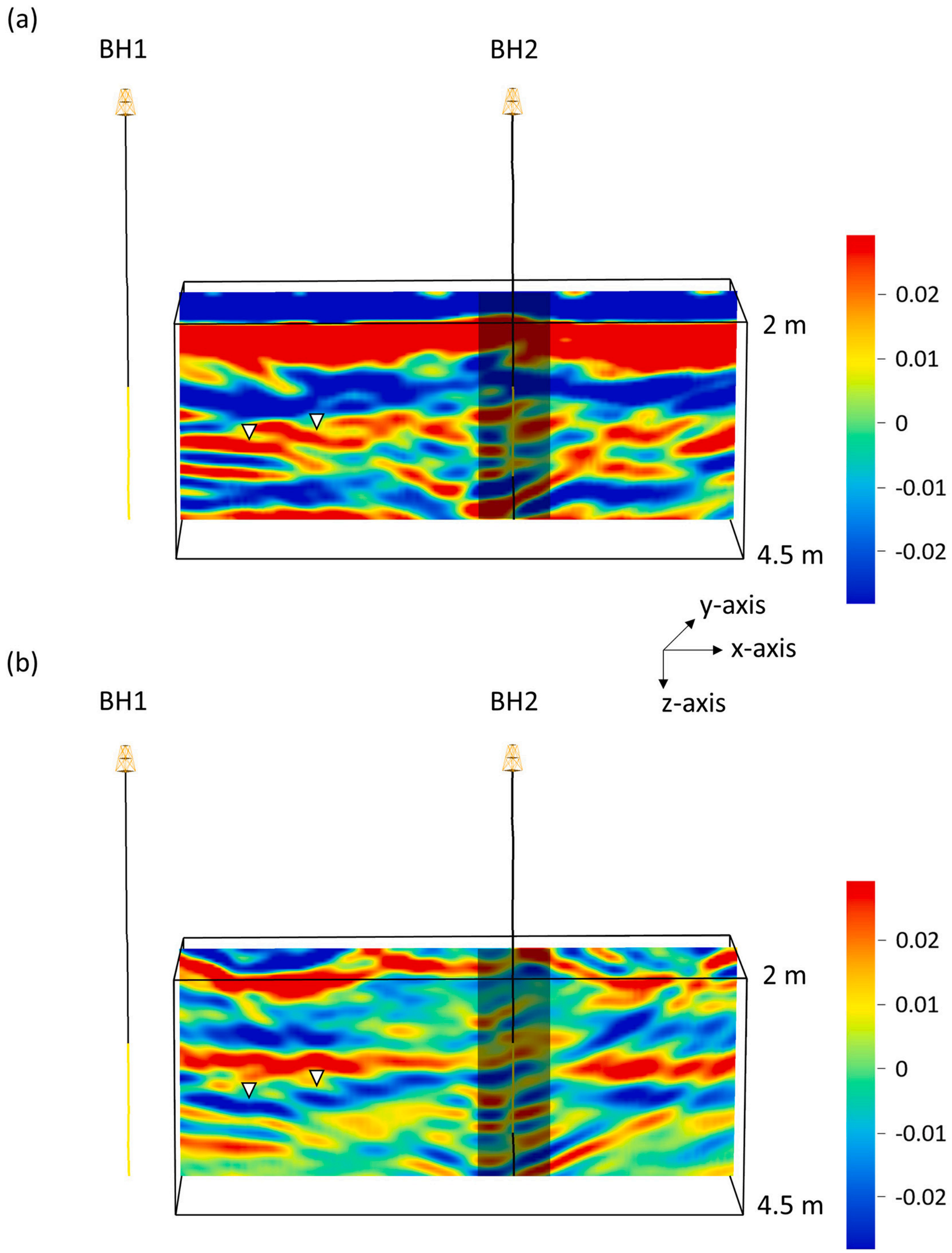

Fig. 5. 3-D migrated 160 MHz data represented by a vertical slice passing through the chosen boreholes. (a) Migration of the processed reference GPR acquisition data (before injection) and (b) migration of differences between acquisition times (final - reference). The shaded area corresponds to the zone above which we did not perform GPR profile surveys. The injection and extraction boreholes are BH2 and BH1, respectively, with the solicited sections highlighted in yellow along the boreholes. The apexes of white triangles indicate the location of observed relative amplitude changes that are analyzed in Section 4.1 (Fig. 6a, b). The amplitudes are unitless and refer to the input data for migration that had normalized magnitudes varying between −1 and 1. (For interpretation of the references to colour in this figure legend, the reader is referred to the web version of this article.)

specify a corresponding electrical dipole at each discretized element of the fracture surface. Subsequently, each such secondary dipole is transmitted to the receiver location using the same analytical solution used for source radiation modeling. By summing the contributions of all secondary dipoles over the discretized fracture at the receiver location, it is possible to simulate the GPR response of fractures with heterogeneous electrical conductivity and permittivity fields very cheaply at high accuracy (Shakas and Linde, 2015; Shakas et al., 2017). Here, we consider a square and homogeneous horizontal fracture with dimension of 2 m situated at 3.6 m depth (similar to the first GPR data reflection analyzed in Fig. 6a, c). The rock matrix is given an electrical conductivity of 2×10^{-4} S/m and relative permittivity of 6. The EC of the fracture-fluid was chosen as 1.8 S/m (corresponding to the saline formation water) and the initial aperture was fixed at 5.7×10^{-5} m (considering a mechanical fracture aperture reaching 8.5×10^{-5} m, calculated during tracer test, and a 50% widening induced by the high-

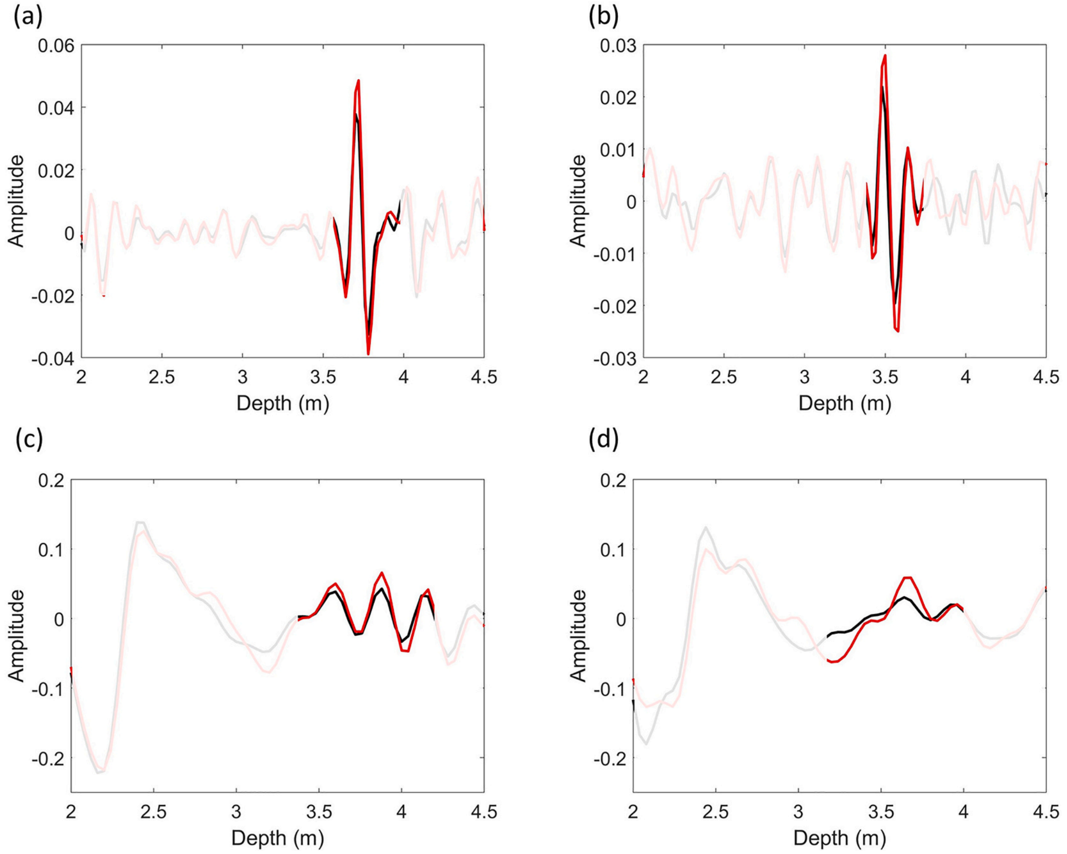

Fig. 6. 3-D Field migrated trace data for (a,b) the 450 MHz and (c,d) the 160 MHz data. Large GPR reflections originated from fractures situated (a,c) at 3.6 m of depth and at 1.14 m away from BH1 and (b,d) at 3.4 m of depth and at 2.18 m away from BH1. These reflections are pointed by white triangles on 2-D vertical slices on Fig. 4 (450 MHz) and Fig. 5 (160 MHz). The signals from reference and final GPR acquisitions are represented in black and red respectively. The amplitudes are unitless and refer to the input data for migration that had normalized magnitudes varying between −1 and 1. (For interpretation of the references to colour in this figure legend, the reader is referred to the web version of this article.)

pressure injection; detailed calculations are shown in supplementary material). The antenna dipole moments are modeled as a generalized gamma distribution (Shakas and Linde, 2015) with frequency spectra that are similar to the observed frequency contents of the 160 MHz and 450 MHz GPR antennas, respectively.

First, we assessed how the GPR signal responds when the EC of the fracture-fluid is reduced in response to the injection of the resistive tracer. To do so, we considered a decrease to EC = 1.0 S/m, which is much lower than the value observed at peak tracer breakthrough of 1.6 S/m in BH1. This is done because dilution in BH1 is expected as it draws water from several fractures, with some of them not being involved in the tracer transport. The modeled 450 MHz (Fig. 7a) and 160 MHz (Fig. 7c) traces show an amplitude decrease of 25% and 35% respectively. Next, we consider the impact of an increase in fracture aperture that might arise in response to high-pressure injection while the electrical conductivity of the formation water was kept fixed at 1.6 S/m. Several tests were made with all leading to amplitude increases. The modeling results for 450 MHz (Fig. 7b) and 160 MHz (Fig. 7d) are given for an aperture increase of 50% leading to corresponding increases of 49% in terms of both peak amplitudes (observed for the first positive peak). By comparing with the actual data in Fig. 6, we see that the chosen scenario of a 50% aperture increase provides similar responses to those being observed. Thus, the observed increases of GPR reflectivity in the stimulated fractures suggest that the observed GPR time-lapse response is dominated by aperture increases due to high injection pressure rather than electrical conductivity decreases due to the injected tracer that tend to decrease reflectivity. Since the tracer injection is expected to decrease the electrical conductivity of the fracture-fluid somewhat, we expect that a slightly lower increase in reflectivity would occur than the one considered in the scenario of an increasing aperture and constant fracture-fluid properties. However, given the important uncertainties involved in the modeling, we refrain from considering a mixed scenario involving increasing aperture and decreasing salinity. We stress that the amplitudes obtained by the difference migrations (Fig. 6) and the modeling results (Fig. 7) are not comparable, while the relative variations in amplitudes are. Indeed, the actual magnitude of the source is unknown and can, thus, not be modeled. In the next section, we assess if the suggested 50% increase in fracture aperture during tracer injection is consistent with hydromechanical considerations.

4.2. Is the hypothesis of a 50% aperture increase compatible with hydromechanics?

The hypothesis that fractures may open up unevenly due to pressure increases in a 450 m deep Äspö tunnel section was investigated by Fransson et al. (2010) based on hydraulic testing and grouting records. The results obtained were less conclusive than for much shallower tunnels (Fransson et al., 2010) and they provide no estimate about aperture variations. In this section, we analyze the present tracer experiment and test whether the 50% increase in aperture suggested by the GPR analysis is consistent with the predicted aperture widening given the pressure change induced by pumping, considering what is known about the hydromechanical behavior of fractured rocks.

Before the injection test, when the first GPR survey was performed, BH1 was at atmospheric pressure and BH2 at ~1800 kPa (Fig. 2a).

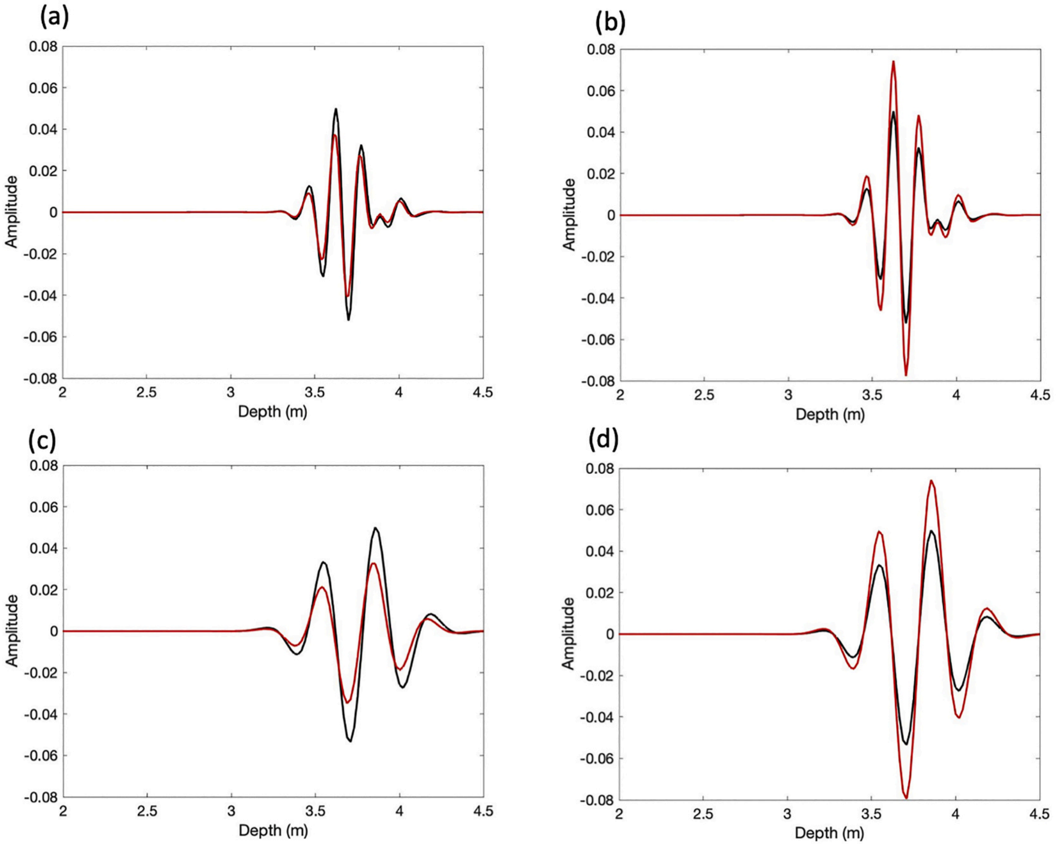

Fig. 7. GPR trace modeling for (a,b) 450 MHz frequency and (c,d) 160 MHz frequency. (a,c) We imposed a decrease of fluid EC filling the fracture with reference trace (black) corresponding to the initial EC at 1.8 S/m and final trace (red) corresponding to the EC at 1.0 S/m (from tracer solution filling BH2 just before injection start); (b,d) we imposed a 50% increase of fracture widening with reference trace (black) corresponding to an aperture of 57 μm and final trace (red) corresponding to an aperture of 85 μm. The focus on the interpretation and the comparison with Fig. 6 should be based on relative magnitude variations; the magnitudes are not comparable as the true source magnitude is unknown. (For interpretation of the references to colour in this figure legend, the reader is referred to the web version of this article.)

During the injection test, the fluid pressure in BH2 increases up to 5000 kPa with no change in BH1. Fig. 8 shows the differential fluid pressure that is assumed to increase linearly between the GPR surveys in the line joining BH1 and BH2 at the injection depth. The total pressure between the fracture walls is expected to decrease by the same value, entailing an increase of the fracture aperture. In the locations where the GPR signals from fractures were analyzed (pointed by white apexes on Figs. 4 and 5), we estimate the decrease of wall pressure (Fig. 8) to be 870 kPa (for the fracture situated at 1.14 m away from BH1; Fig. 6a, c) and 1700 kPa (for the fracture situated at 2.18 m away from BH1; Fig. 6b, d).

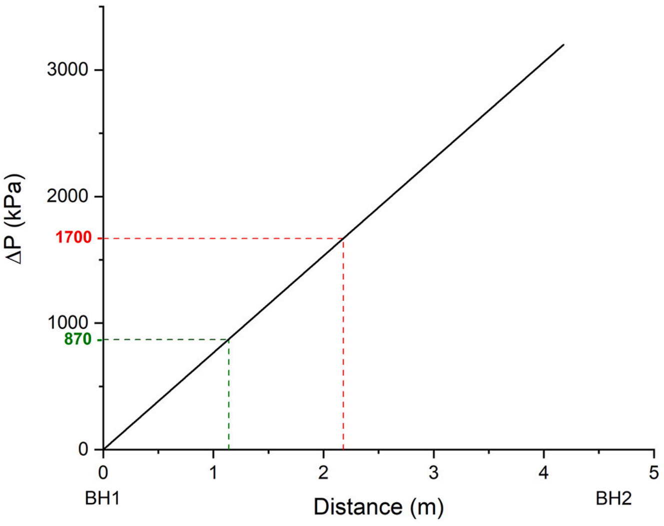

Fig. 8. Pressure differences between boreholes (BH1 and BH2) between reference and final GPR acquisitions. The pressure differences indicated in green and red are situated at the analyzed GPR signals located 1.14 and 2.18 m away from BH1. (For interpretation of the references to colour in this figure legend, the reader is referred to the web version of this article.)

The variation of fracture aperture due to pressure change can be predicted either from the rock compressibility or the fracture stiffness. Rock compressibility of granitic or hardrock geological formations is commonly very low when measured on small unfractured (or microfractured) laboratory samples, generally of the order of 1/(10 GPa) at ambient pressure down to 1/(100 GPA) at high pressure (Brace, 1965). At pressures below 100 MPa, fractures play a dominant role in the compressibility of hard rocks and most of the rock deformation is concentrated in or around fractures (Walsh, 1965; Walsh and Grosenbaugh, 1979). By assuming that most of the deformation results from a change in aperture, a change of the rock mass volume V is $\Delta V = \Delta\bar{a}\, p_{32}\, V$, where p_{32} is the total surface of fractures per unit volume and $\Delta\bar{a}$ the variation of the average fracture aperture over the fracture network. Furthermore, p_{32} is related to the average aperture $\bar{a}$ and to the total rockmass porosity ϕ by $\phi = \bar{a}\, p_{32}$. The average aperture variation can then be calculated from:

$$\frac{\Delta\bar{a}}{\bar{a}} = \frac{1}{\phi}\frac{\Delta V}{V} = \frac{\beta_r}{\phi}\Delta P, \tag{1}$$

with β_r the bulk rock mass compressibility at the scale of interest. The total porosity for Äspö rocks has been measured to be around 0.2–0.3% (Autio et al., 2003) and β_r estimated for rock samples with microcracks at about 1/(40 ± 10 GPa) as derived from the bulk modulus given by Hakami et al. (2008). This results in a ratio $\frac{\beta_r}{\phi}$ of 1/(120±40 MPa) resulting in a change that is less than 1% for a pressure increase of 1 MPa, that is, much less than the values estimated from the GPR modeling. The problem with the preceding analysis is that the elastic constants are not measured at the right scale, and not for the type of fractures that are imaged by GPR. For fractured rocks, we expect the Young and bulk modulus to decrease when increasing the rock mass scale, entailing an increase in compressibility (Davy et al., 2018). Values of compressibility as low as 1/(5 GPa) have been reported by Zangerl et al. (2008b) to explain the surface subsidence associated with highway tunneling in the fractured crystalline Gotthard massif (Switzerland), which would result in an aperture variation that is compatible with that predicted by the GPR data.

Another approach to estimate the aperture variation can be achieved from the normal fracture stiffness k_n:

$$\frac{\Delta a}{a} = \frac{\Delta P}{k_n a}. \tag{2}$$

This requires estimating both the initial aperture a and the normal stiffness k_n. The former can be deduced from hydraulic testing, either by converting transmissivity values into equivalent “hydraulic” aperture through the cubic law (Tsang and Witherspoon, 1981; Witherspoon et al., 1980), or by inferring it from tracer tests (derived from Thiem’s solution (Thiem, 1906)). The hydraulic aperture was estimated at about 12 μm and the mechanical aperture from tracer data at about 85 μm (see supplementary material), the latter being the most appropriate estimate of mechanical aperture (Tsang, 1992). Estimating the normal stiffness is challenging since k_n is not an intrinsic property of the material but depends on the effective normal stress and likely also on the fracture size. Direct measurements from grouting data gives values of 35 GPa/m and 600 GPa/m for two boreholes at 450 m depth in the Äspö tunnel (Fransson et al., 2010). The smaller value for k_n gives an aperture variation of ~35% for a pressure change of 1 MPa. Other estimates of k_n have been reviewed by Zangerl et al. (2008a) by using the semi-logarithmic closure law between aperture and effective stress $\sigma_n{}'$, $-\Delta a = a(\sigma_o^{'}) - a(\sigma_n^{'}) = a_c ln\left(\frac{\sigma_n^{'}}{\sigma_o^{'}}\right)$, developed by Walsh and Grosenbaugh (1979) for the closure of surfaces whose topography is characterized by an exponential distribution of summit asperity heights. Zangerl et al. (2008a) compiled values of the ‘stiffness characteristic’ (a_c^{-1}), which leads to a_c ranging from 10 μm to 100 μm for granite samples of different sizes (up to 3 m) and corresponding relative fracture variations of 20–200%.

Considering the uncertainty on hydromechanical parameters, we conclude that the aperture variation inferred by GPR is not inconsistent with hydromechanical parameters. Larger scale in situ experiments as those presented herein for GPR is a good way forward to obtain better estimates of in-situ elastic parameters at the scale of interest (e.g., Zangerl et al. (2008a) and Zangerl et al. (2008b)).

5. Conclusion

GPR data acquired during high-pressure injection of a resistive tracer were used to image fracture connectivity and induce aperture variations between two boreholes (BH1 and BH2). The experiment was performed in fractured rock of very low permeability a few meters beneath a tunnel situated at 410 m depth. We injected the tracer solution (Uranine + deionized water) with constant high-pressure in a convergent-dipole geometry. To image the tracer pathways, we performed 3-D surface-based GPR. GPR reflections in very low permeable environments with sub-mm fracture aperture are weak. Nevertheless, the difference of the final with respect to the reference GPR acquisition data provides a response that is consistent with the tracer injection depth, particularly for the higher-quality 450 MHz data that only show difference signals related to the depth interval of the tracer injection. The observed 45% increase in fracture reflectivity is reproduced by GPR-modeling when considering a 50% increase in fracture aperture, while a decrease in salinity due to the tracer injection leads to a smaller decrease in reflectivity (25%). Considering the large uncertainty in hydromechanical parameters at the site, we find that a 50% increase in aperture in response to the injection pressure is compatible with hydromechanical considerations. This suggests that information on aperture variations provided by field-scale in situ GPR experiments during hydraulic stimulation could help to better estimate elastic parameters of the studied fractured rock. Given the low injection rate of 8.6 mL/min, we were unable to significantly change the electrical properties of the fluid-filled fractures in this formation of very low permeability (hydraulic fracture aperture of 12 μm). This limits the practical applicability of time-lapse GPR-assisted tracer-monitoring in the development of nuclear waste repositories. Our injection experiment also highlights challenges when high injection pressures are needed to observe clear measurement responses, as the induced fracture widening leads to an upward bias on transmissivity estimates with associated implications for risk assessments.

Declaration of Competing Interest

The authors declare that they have no known competing financial interests or personal relationships that could have appeared to influence the work reported in this paper.

Acknowledgements

ENIGMA ITN project that has received funding from the European Union’s Horizon 2020 Research and Innovation Programme under the Marie Sklodowska-Curie Grant Agreement No 722028. Furthermore, we received significant financial support from SKB. The data used for this study are stored in the Sicada database and are available by an official request to the company. We would like to thank Lars Andersson, Patrik Vidstrand and Siren Bortelid Robertsson (SKB) and Peter Andersson and Johanna Ragvald (Geosigma) for their technical support and quality fieldwork. We also thank Diego Mas Ivars (SKB) for important input in terms of hydromechanics, Christian Le Carlier De Veslud (Géosciences Rennes) for his support with the use of Paradigm GOCAD™ and Silvia De Simone for her help with the different aperture estimations. This study is also supported by the French National Observatory H+. The GPR and tracer tests data are available at http://hplus.ore.fr/en/molron-et-al-2021-eg-data and, after a requesting login through http://hplus.ore.fr/en/database/acces-database. Constructive reviews from two anonymous reviewers and Editor Wasowski helped to significantly improve our manuscript.

Appendix A

References

Andersson, P., Ragvald, J., 2021. ENIGMA Project - GPR monitoring of fractures at Äspö HRL. In: Results of Field Investigations in TAS04, SKB Report P-19-17. Svensk Kärnbränslehantering AB.

Autio, J., Hjerpe, T., Siitari-Kauppi, M.K., 2003. Porosity, diffusivity and permeability of EDZ in crystalline rock and effect on the migration in a KBS-3 type repository. In: Paper Presented at the CLUSTER Conference Held in Luxembourg on 3-5 November 2003.

Becker, M., Tsoflias, G., 2010. Comparing flux-averaged and resident concentration in a fractured bedrock using ground penetrating radar. Water Resour. Res. 46 (9) https://doi.org/10.1029/2009WR008260.

Brace, W.F., 1965. Some new measurements of linear compressibility of rocks. J. Geophys. Res. 70 (2), 391–398. https://doi.org/10.1029/JZ070i002p00391.

Cosma, C., Olsson, O., Keskinen, J., Heikkinen, P., 2001. Seismic characterization of fracturing at the Äspö Hard Rock Laboratory, Sweden, from the kilometer scale to the meter scale. Int. J. Rock Mech. Min. 38 (6), 859–865. https://doi.org/10.1016/S1365-1609(01)00051-X.

CREWES, 1988. CREWES Matlab Toolbox. https://www.crewes.org/ResearchLinks/FreeSoftware/ (accessed 20 November 2017).

Davison, C.C., Brown, A., Everitt, R.A., Gascoyne, M., Kozak, E.T., Lodha, G.S., Martin, C. D., Soonawala, N.M., Stevenson, D.R., Thorne, G.A., 1994. The Disposal of Canada's Nuclear Fuel Waste: Site Screening and Site Evaluation Technology, (AECL-10719, COG-93-3). Retrieved from. Whiteshell Laboratories, Pinawa, MB, Canada.

Davy, P., Darcel, C., Le Goc, R., Mas Ivars, D., 2018. Elastic properties of fractured rock masses with frictional properties and power law fracture size distributions. J. Geophys. Res. Solid Earth 123 (8), 6521–6539. https://doi.org/10.1029/2017JB015329.

Day-Lewis, F.D., Lane, J.W., Harris, J.M., Gorelick, S.M., 2003. Time-lapse imaging of saline-tracer transport in fractured rock using difference-attenuation radar tomography. Water Resour. Res. 39 (10) https://doi.org/10.1029/2002wr001722.

Day-Lewis, F.D., Slater, L.D., Robinson, J., Johnson, C.D., Terry, N., Werkema, D., 2017. An overview of geophysical technologies appropriate for characterization and monitoring at fractured-rock sites. J. Environ. Manag. 204, 709–720. https://doi.org/10.1016/j.jenvman.2017.04.033.

Dorn, C., Linde, N., Doetsch, J., Le Borgne, T., Bour, O., 2011a. Fracture imaging within a granitic rock aquifer using multiple-offset single-hole and cross-hole GPR reflection data. J. Appl. Geophys. 78, 123–132. https://doi.org/10.1016/j.jappgeo.2011.01.010.

Dorn, C., Linde, N., Le Borgne, T., Bour, O., Baron, L., 2011b. Single-hole GPR reflection imaging of solute transport in a granitic aquifer. Geophys. Res. Lett. 38 (8) https://doi.org/10.1029/2011gl047152.

Ericsson, L., Vidstrand, P., Christiansson, R., Morosini, M., 2018. Comparison Between Blasting and Wire Sawing Regarding Hydraulic Properties of the Excavated Damaged Zone in a Tunnel–Experiences From Crystalline Rock at the Äspö Hard Rock Laboratory, Sweden. Paper presented at the 52nd US Rock Mechanics/Geomechanics Symposium.

Ericsson, L.R.C., Lehtimäki, T., Ittner, H., Hansson, K., Butron, C., Sigurdsson, O., Kinnbom, P., 2015. A Demonstration Project on Controlling and Verifying the Excavation-Damaged Zone, (R-14-30). Retrieved from Stockholm, Sweden.

Fransson, Å., Tsang, C.-F., Rutqvist, J., Gustafson, G., 2010. Estimation of deformation and stiffness of fractures close to tunnels using data from single-hole hydraulic testing and grouting. Int. J. Rock Mech. Min. 47 (6), 887–893. https://doi.org/10.1016/j.ijrmms.2010.05.007.

Giertzuch, P.-L., Doetsch, J., Jalali, M., Shakas, A., Schmelzbach, C., Maurer, H., 2020. Time-lapse ground penetrating radar difference reflection imaging of saline tracer flow in fractured rock. Geophysics 85 (3), H25–H37. https://doi.org/10.1190/geo2019-0481.1.

Gudmundsson, A., 2011. Rock Fractures in Geological Processes. Cambridge University Press, Cambridge University, New York.

Hakami, E., Fredriksson, A., Lanaro, F., Wrafter, J., 2008. Rock Mechanics Laxemar: Site Descriptive Modelling SDM-Site Laxemar (R-08-57). Retrieved from Stockholm, Sweden.

Hammarström, M., Olsson, O., 1996. Äspö Hard Rock Laboratory. 10 years of Research. Svensk Kärnbränslehantering AB, Sweden.

Klepikova, M.V., Le Borgne, T., Bour, O., Dentz, M., Hochreutener, R., Lavenant, N., 2016. Heat as a tracer for understanding transport processes in fractured media: Theory and field assessment from multiscale thermal push-pull tracer tests. Water Resour. Res. 52 (7), 5442–5457. https://doi.org/10.1002/2016WR018789.

Margrave, G.F., Lamoureux, M.P., 2019. Numerical Methods of Exploration Seismology: With Algorithms in MATLAB®. Cambridge University Press.

McEwen, T., Äikäs, T., 2000. The Site Selection Process for a Spent Fuel Repository in Finland. In: Summary report (POSIVA 2000–15). Retrieved from Helsinki, Finland.

Milnes, A.G., 2002. Swedish deep repository siting programme. In: Guide to the Documentation of 25 years of Geoscientific Research (1976–2000), (TR-02-18). Stockholm, Sweden. Retrieved from.

Molron, J., Linde, N., Baron, L., Selroos, J.-O., Darcel, C., Davy, P., 2020. Which fractures are imaged with Ground Penetrating Radar? Results from an experiment in the Äspö Hardrock Laboratory, Sweden. Eng. Geol. 273 https://doi.org/10.1016/j.enggeo.2020.105674.

National Research Council, 1996. Rock Fractures and Fluid Flow: Contemporary Understanding and Applications. National Academies Press.

Neuman, S.P., 2005. Trends, prospects and challenges in quantifying flow and transport through fractured rocks. Hydrogeol. J. 13 (1), 124–147. https://doi.org/10.1007/s10040-004-0397-2.

Rutqvist, J., Noorishad, J., Tsang, C.F., Stephansson, O., 1998. Determination of fracture storativity in hard rocks using high-pressure injection testing. Water Resour. Res. 34 (10), 2551–2560. https://doi.org/10.1029/98WR01863.

Selroos, J.O., Walker, D.D., Ström, A., Gylling, B., Follin, S., 2002. Comparison of alternative modelling approaches for groundwater flow in fractured rock. J. Hydrol. 257 (1–4), 174–188. https://doi.org/10.1016/S0022-1694(01)00551-0.

Shakas, A., Linde, N., 2015. Effective modeling of ground penetrating radar in fractured media using analytic solutions for propagation, thin-bed interaction and dipolar scattering. J. Appl. Geophys. 116, 206–214. https://doi.org/10.1016/j.jappgeo.2015.03.018.

Shakas, A., Linde, N., 2017. Apparent apertures from ground penetrating radar data and their relation to heterogeneous aperture fields. Geophys. J. Int. 209 (3), 1418–1430. https://doi.org/10.1093/gji/ggx100.

Shakas, A., Linde, N., Baron, L., Bochet, O., Bour, O., Le Borgne, T., 2016. Hydrogeophysical characterization of transport processes in fractured rock by combining push-pull and single-hole ground penetrating radar experiments. Water Resour. Res. 52 (2), 938–953. https://doi.org/10.1002/2015WR017837.

Shakas, A., Maurer, H., Giertzuch, P.L., Hertrich, M., Giardini, D., Serbetto, F., Meier, P., 2020. Permeability enhancement from a hydraulic stimulation imaged with Ground Penetrating Radar. Geophys. Res. Lett. 47 (17) https://doi.org/10.1029/2020GL088783.

SKB, 2016. Äspö Hard Rock Laboratory - Annual Report 2015 (TR-16-10). Retrieved from. Stockholm, Sweden.

Talley, J., Baker, G.S., Becker, M.W., Beyrle, N., 2005. Four dimensional mapping of tracer channelization in subhorizontal bedrock fractures using surface ground penetrating radar. Geophys. Res. Lett. 32 (4) https://doi.org/10.1029/2004GL021974.

Thiem, G., 1906. Hydrologische Methoden, Gebhardt, Leipzig. Germany.

Tsang, C.F., Neretnieks, I., 1998. Flow channeling in heterogeneous fractured rocks. Rev. Geophys. 36 (2), 275–298. https://doi.org/10.1029/97RG03319.

Tsang, Y., 1992. Usage of "equivalent apertures" for rock fractures as derived from hydraulic and tracer tests. Water Resour. Res. 28 (5), 1451–1455. https://doi.org/10.1029/92WR00361.

Tsang, Y., Tsang, C., 1989. Flow channeling in a single fracture as a two-dimensional strongly heterogeneous permeable medium. Water Resour. Res. 25 (9), 2076–2080. https://doi.org/10.1029/WR025i009p02076.

Tsang, Y.W., Witherspoon, P., 1981. Hydromechanical behavior of a deformable rock fracture subject to normal stress. J. Geophys. Res. Solid Earth 86 (B10), 9287–9298. https://doi.org/10.1029/JB086iB10p09287.

Tsoflias, G.P., Becker, M.W., 2008. Ground-penetrating-radar response to fracture-fluid salinity: why lower frequencies are favorable for resolving salinity changes. Geophysics 73 (5), J25–J30. https://doi.org/10.1190/1.2957893.

Tsoflias, G.P., Halihan, T., Sharp, J.M., 2001. Monitoring pumping test response in a fractured aquifer using ground-penetrating radar. Water Resour. Res. 37 (5), 1221–1229. https://doi.org/10.1029/2000wr900297.

Walsh, J., 1965. The effect of cracks on the compressibility of rock. J. Geophys. Res. 70 (2), 381–389. https://doi.org/10.1029/JZ070i002p00381.

Walsh, J., Grosenbaugh, M., 1979. A new model for analyzing the effect of fractures on compressibility. J. Geophys. Res. Solid Earth 84 (B7), 3532–3536. https://doi.org/10.1029/JB084iB07p03532.

Witherspoon, P.A., Wang, J.S., Iwai, K., Gale, J.E., 1980. Validity of cubic law for fluid flow in a deformable rock fracture. Water Resour. Res. 16 (6), 1016–1024. https://doi.org/10.1029/WR016i006p01016.

Zang, A., Stephansson, O., Stenberg, L., Plenkers, K., Specht, S., Milkereit, C., Schill, E., Kwiatek, G., Dresen, G., Zimmermann, G., Dahm, T., Weber, M., 2016. Hydraulic fracture monitoring in hard rock at 410 m depth with an advanced fluid-injection protocol and extensive sensor array. Geophys. J. Int. 208 (2), 790–813. https://doi.org/10.1093/gji/ggw430.

Zangerl, C., Eberhardt, E., Evans, K., Loew, S., 2008a. Consolidation settlements above deep tunnels in fractured crystalline rock: part 2—Numerical analysis of the Gotthard highway tunnel case study. Int. J. Rock Mech. Min. 45 (8), 1211–1225. https://doi.org/10.1016/j.ijrmms.2008.02.005.

Zangerl, C., Evans, K., Eberhardt, E., Loew, S., 2008b. Consolidation settlements above deep tunnels in fractured crystalline rock: part 1—Investigations above the Gotthard highway tunnel. Int. J. Rock Mech. Min. 45 (8), 1195–1210. https://doi.org/10.1016/j.ijrmms.2008.02.002.